



A flexible design framework to design graded porous bone scaffolds with adjustable anisotropic properties

K. Cheikho, J.F. Ganghoffer, A. Baldit, E. Labbé, S. Alix, H. Kerdjoudj, C. Mauprivez, A. Lebée, Cédric P. Laurent

► To cite this version:

K. Cheikho, J.F. Ganghoffer, A. Baldit, E. Labbé, S. Alix, et al.. A flexible design framework to design graded porous bone scaffolds with adjustable anisotropic properties. *Journal of the mechanical behavior of biomedical materials*, 2023, 140, pp.105727. 10.1016/j.jmbbm.2023.105727 . hal-04016453

HAL Id: hal-04016453

<https://hal.science/hal-04016453>

Submitted on 8 Mar 2023

HAL is a multi-disciplinary open access archive for the deposit and dissemination of scientific research documents, whether they are published or not. The documents may come from teaching and research institutions in France or abroad, or from public or private research centers.

L'archive ouverte pluridisciplinaire **HAL**, est destinée au dépôt et à la diffusion de documents scientifiques de niveau recherche, publiés ou non, émanant des établissements d'enseignement et de recherche français ou étrangers, des laboratoires publics ou privés.

A flexible design framework to design graded porous bone scaffolds with adjustable anisotropic properties

K. Cheikho^{a,*}, J.F. Ganghoffer^a, A. Baldit^a, E. Labbé^b, S. Alix^b, H. Kerdjoudj^c, C. Mauprivez^c, A. Lebé^d, C. Laurent^a

^a CNRS UMR 7239 LEM3 - Université de Lorraine, Nancy, France

^b Université de Reims Champagne Ardenne, ITheMM EA 7548, 51097 Reims, France

^c Université de Reims Champagne Ardenne, BIOS EA 4691, 51097 Reims, France

^d Navier UMR 8205, Ecole des Ponts ParisTech, Université Gustave Eiffel, CNRS, Marne-la-Vallée, France

* corresponding author

Abstract

Since the success of bone regenerative medicine depends on scaffold morphological and mechanical properties, numerous scaffolds designs have been proposed in the last decade, including graded structures that are suited to enhance tissue ingrowth. Most of these structures are based either on foams with a random pore definition, or on the periodic repetition of a unit cell (UC). These approaches are limited by the range of target porosities and obtained effective mechanical properties, and do not permit to easily generate a pore size gradient from the core to the periphery of the scaffold. In opposition, the objective of the present contribution is to propose a flexible design framework to generate various three-dimensional (3D) scaffolds structures including cylindrical graded scaffolds from the definition of a UC by making use of a non-periodic mapping. Conformal mappings are firstly used to generate graded circular cross-sections, while 3D structures are then obtained by stacking the cross-sections with or without a twist between different scaffold layers. The effective mechanical properties of different scaffold configurations are presented and compared using an energy-based efficient numerical method, pointing out the versatility of the design procedure to separately govern longitudinal and transverse anisotropic scaffold properties. Among these configurations, a helical structure exhibiting couplings between transverse and longitudinal properties is proposed and permits to extend the adaptability of the proposed framework. In order to investigate the capacity of common additive manufacturing techniques to fabricate the proposed structures, a subset of these configurations is elaborated using a standard SLA setup, and subjected to experimental mechanical testing. Despite observed geometric differences between the initial design and the actual obtained structures, the effective properties are satisfyingly predicted by the proposed computational method. Promising perspectives are offered concerning the design of self-fitting scaffolds with on-demand properties depending on the clinical application.

© 2012 Published by Elsevier Ltd. Selection and/or peer-review under responsibility of Global Science and Technology Forum Pte Ltd

Keywords: Graded scaffolds; Finite element method; Bone repair; Stereolithography; Open-cell structures; additive manufacturing ; material by design ; metamaterials.

1. Introduction

The selection of a suited scaffold geometry constitutes a milestone in bone repair, with a wide variety of proposed shapes and microstructures (Patrick et al., 1998). Bone scaffolds are based on a biocompatible biomaterial, natural or synthetic, used temporarily or permanently, and should be porous, permeable and three-dimensional (3D) (Payne et al., 2014). It must promote cell adhesion, the development of a newly formed tissue (Nair et al., 2007), and ideally mimic the mechanical properties of the host bone (Afshar et al., 2016; Li et al., 2006). Scaffold designs should also be adapted to the future anatomical site of implantation (Afshar et al., 2016; Torres-Sanchez et al., 2017) and to the associated planned surgical protocol, with a growing interest for minimally-invasive surgeries (Di et al., 2016; Langford et al., 2021). The list of key requirements to be fulfilled when designing a scaffold for bone repair includes the biocompatibility of the constitutive material (Qu et al., 2019) and its osseoregenerative properties (Ghassemi et al., 2018), as well as morphological properties such as mean pore size (Torres-Sanchez et al., 2017), porosity (Bandyopadhyay et al., 2010), pore interconnectivity (Jones et al., 2009) and distribution of porosities (Poh et al., 2019) suited to create an optimal environment for bone ingrowth (Bobbert and Zadpoor, 2017; Dias et al., 2012; Jungreuthmayer et al., 2009; Karageorgiou and Kaplan, 2005; Zadpoor, 2015). In terms of mechanical properties, the scaffold should be able to withstand external loads, and it is generally assumed that it must mimic the initial mechanical physiological functions of the bone tissue (Afshar et al., 2016). In the context of bone regenerative medicine, one additional challenge may consist in mimicking the natural vascularization of bone (He et al., 2013; Logeart-Avramoglou et al., 2005) since insufficient growth of microvessels can lead to local morbidity and reduce the clinical success of bone repair by limiting interstitial fluid diffusion, blood perfusion, and cellular waste removal (Brennan et al., 2013; Melchiorri et al., 2014). The risk of insufficient vascularization is particularly important in thick, three-dimensional samples, since initial natural diffusion is not possible beyond 100µm matrix thickness (Karageorgiou and Kaplan, 2005; Oh et al., 2007) and cell death then rapidly occurs by poor oxygenation in the center of the implant (Brennan et al., 2013; Leszczynska et al., 2013). This requirement is less important for very small fillings (Payne et al., 2014).

In the last decade, there have been numerous propositions of design strategies for the development of devices with tailored morphology and integrated functionalities (Guarino et al., 2012) or to help the design of prostheses for different types of tissues (e.g. (Jackson, 2021)). Scaffolds can be made from a variety of materials, including natural polymers, synthetic polymers, and ceramics, and can be designed to mimic the structure and function of native tissue. Some of these approaches have been used successfully to develop a wide range of devices with tailored morphology and integrated functionalities, and continue to be an active area of research and development. The proposition of innovative design frameworks that could extend the range of reachable properties for such structures still constitutes a major point of interest in the field of regenerative medicine. The emergence of additive manufacturing has permitted to design various scaffold architectures, essentially based on the 3D periodic repetition of a unit cell (UC) to form porous 3D structures (Afshar et al., 2016; Bahraminasab, 2020; Bobbert and Zadpoor, 2017; Deng et al., 2021; Dias et al., 2012; Donate et al., 2020; Fernandes et al., 2020; Kolken et al., 2020; Liu et al., 2018; Su et al., 2021; Wang et al., 2020; Yoo, 2011). As a consequence of this periodic design framework, the resulting 3D porous scaffolds generally exhibit isotropic properties, while native bone tissue is far from being isotropic (Li et al., 2013) and anisotropic behavior may be suited for specific applications (Rüegg et al., 2017). In opposition to these perfectly periodic structures, it has been reported that scaffolds with pore size gradients offer better seeding efficiency than homogeneous scaffolds (Sobral et al., 2011) and enhance the diffusion of nutrients from the core to the periphery of scaffolds (Ahn et al., 2010). As a result of these observations, various heterogeneous geometries with pore size gradients have been proposed in order to counter the limited proliferation and vascularization of 3D scaffolds observed for

large bone defects (Afshar et al., 2016; Cheikho et al., 2022; Liu et al., 2018; Melchels et al., 2010; Poh et al., 2019; Yook et al., 2012).

In the case of perfectly periodic structures, homogenization techniques have been used to compute the effective properties of porous scaffolds prior to their fabrication from the definition of the UC (Dias et al., 2012; Lin et al., 2004; Shipley et al., 2009). Notably, such homogenization procedures have highlighted the wide range of 2D effective elastic properties that can be obtained from different UC's (Karathanasopoulos et al., 2018). The development of micromechanical models may also result in the effective properties of periodic heterogeneous media (Ganghoffer and Reda, 2021; Louna et al., 2019). However, most of these techniques are currently limited to perfectly periodic structures and cannot predict the mechanical properties of graded scaffolds, though some extensions have been recently proposed for quasi-periodic structures (Andrianov et al., 2006; Le and Marigo, 2018; Miedzińska, 2017; Xu and Qian, 2021). Moreover, homogenization methods are based on the assumption of a scale separation between the macroscale of the scaffold and the microscale of the UC, while in the case of bone scaffold design such an assumption may be debatable (pore sizes on the range of 300-400 μm for bone tissue (Oh et al., 2007) within centimeter-size scaffolds). Alternatively, from the definition of scaffold geometry issued from computed aided design (CAD), energy-based methods (identifying macroscopic energy density stored in a homogeneous equivalent media with the sum of microscopic energy density) have recently allowed for the efficient computation of the effective properties of heterogeneous media (Ayad et al., 2020; Goda et al., 2016; Goda and Ganghoffer, 2015).

In a recent study (Cheikho et al., 2022), an original framework has been proposed to design graded circular porous architectures based on different mappings of a UC, as well as an efficient energy-based method to compute the effective mechanical properties of the resulting structures. However, this preliminary study suffers from several limitations: firstly, it is limited to the design of two-dimensional (2D) scaffold cross-sections, while 3D porous structures are needed for bone regeneration. Secondly, no experimental validation is provided to corroborate the results of the developed numerical method. Lastly, the observed effective properties are conditioned to the fact that additive manufacturing techniques are able to reconstitute the precise geometry of the proposed architectures, since strains may be concentrated in fine junctions. In response to these limitations, the first objective of the present contribution was to extend the work reported previously to 3D porous scaffolds by adding different types of linking elements between the 2D cross-sections, in order to generate anisotropic porous 3D scaffolds with adjustable transverse and longitudinal mechanical properties. The reported energy-based computational method used to predict effective mechanical properties was then extended to these 3D structures to investigate the range of reachable apparent mechanical properties, with a focus on some particular UC's as an illustration of the method. The second objective was to evaluate the feasibility of fabricating such structures using stereolithography (SLA), by comparing the obtained geometry issued from microtomography (μCT) with the initial geometry issued from CAD. SLA was selected among others additive manufacturing techniques, since it has now largely reached the clinical stage and daily dentist's practice (Tian et al., 2021), and it has been successfully used for various clinical applications (Chartrain et al., 2018; Tian et al., 2021). It offers a better resolution than the more common Fused Filament Fabrication (FFF) technique (Peltola et al., 2008), and it is currently extended to a broadening number of compatible materials in order to widen the range of clinical applications of SLA in regenerative medicine. The third and last objective of the present contribution was to confront some of the predicted effective mechanical properties of the scaffold to experimental data, by performing axial and transverse mechanical testing on printed structures.

2. Materials and methods

2.1. Design of 3D scaffold

In our recent work (Cheikho et al., 2022), we proposed a new method to design various scaffolds cross-sections based on the 2D mapping of various UC's. The large range of reachable apparent mechanical properties of the generated cross-sections, depending on the selected UC and the chosen mapping, were particularly underlined. In this first study, based on a given UC (for instance, the hexachiral (HC) unit cell illustrated in Fig. 1.a), periodic (PT) or circular transformations (CT) were used to generate cross-sections, as illustrated in Fig. 1.b. and Fig. 1.c respectively. As observed in the same figure, the CT transformation resulted in graded cross-sections with a pore size gradient from the core to the periphery of the scaffold. Based on this first study, it was observed that UC consisting in a square cell with a circular hole (named SC hereafter) led to highest transverse compressibility within the set of selected UC, while the HC cell was associated to the lowest transverse compressibility due to its auxetic nature. In the subsequent developments, these two types of UC (SC and HC) associated with the two aforementioned mappings (PT and CT) were used. The proposed framework may however easily be extended to other types of UC's and mappings. As an example, the HC-PT cross-section illustrated in Fig. 1.c corresponds to a circular transformation applied on a hexachiral UC.

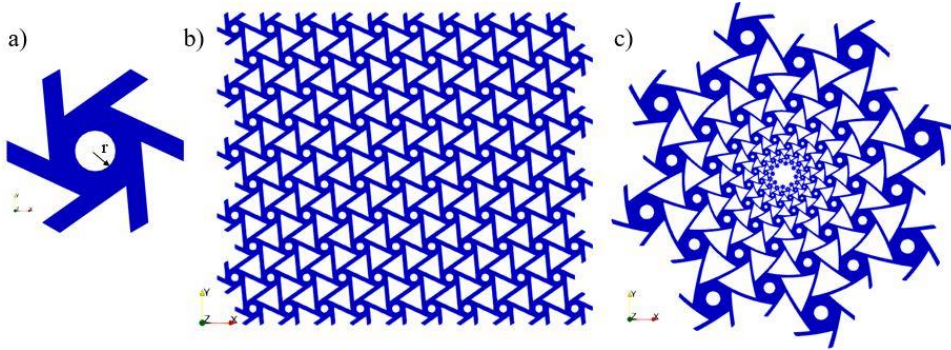


Fig. 1. a) Hexachiral (HC) unit cell (UC), b) Periodic transformation of Hexachiral UC (HC-PT), c) Circular transformation of Hexachiral UC (HC-CT)

This method was obviously limited to 2D in our former study, while 3D porous structures may be obtained from a stacking of such cross-sections in the longitudinal direction. To do so, an initial extrusion of the cross-section with a given thickness was performed in order to form a 3D layer, and cylindrical longitudinal linking elements were then added in the centered holes of the UC in order to create an elementary stack. The multilayer repetition of this step enabled to generate 3D porous scaffolds, as illustrated in Fig. 2.a. and Fig. 2.b. from PT and CT mappings respectively for a HC cell, and in Fig. 3.a. and Fig. 3.b. from PT and CT mappings respectively for a SC cell. This method obviously preserved the mechanical properties of the linking elements along the z -direction, *i.e.* the longitudinal compression stiffness of the resulting scaffold was expected to be equal to the sum of the stiffnesses of these individual elements. Alternatively, in order to control the compressive behavior of the resulting scaffold in the longitudinal direction, the linking elements may be generated with an angle between two layers: by restricting this design method to a single and constant angle throughout the stack of different layers, helical scaffolds were obtained as illustrated in in Fig. 2.c and Fig. 3.c for HC and SC unit cells respectively, showing an overall twist angle of $\pi/2$. In the sequel, the helical structure resulting from CT with inclined linking elements will be denoted HCT. At the end of this design procedure, the obtained structures depend on the UC definition, the parameters of the transformation, the thickness of layers, and the diameter,

length and inclination of linking elements. The overall porosity was a consequence of the combination of these parameters, and was fixed at 74 % as illustrated in Fig. 2 and Fig. 3. Porosity was computed from the ratio between the actual volume of the generated solid and the volume of the equivalent cylindrical continuum.

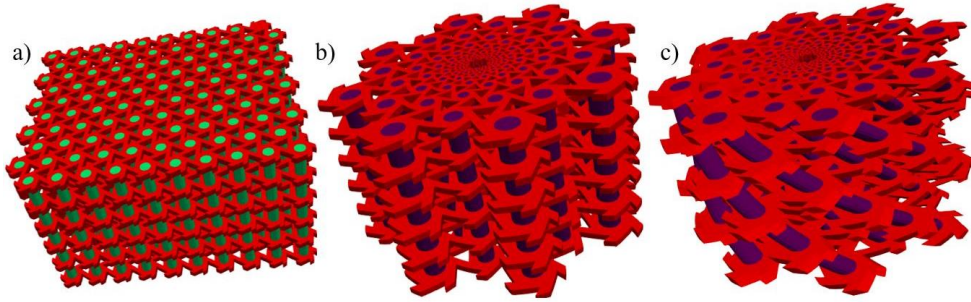


Fig. 2. Mapping of Hexachiral UC with a given porosity of 74 % a) Periodic transformation HC-PT, b) Circular transformation with vertical linking elements HC-CT, c) Circular transformation with inclined linking elements HC-HCT.

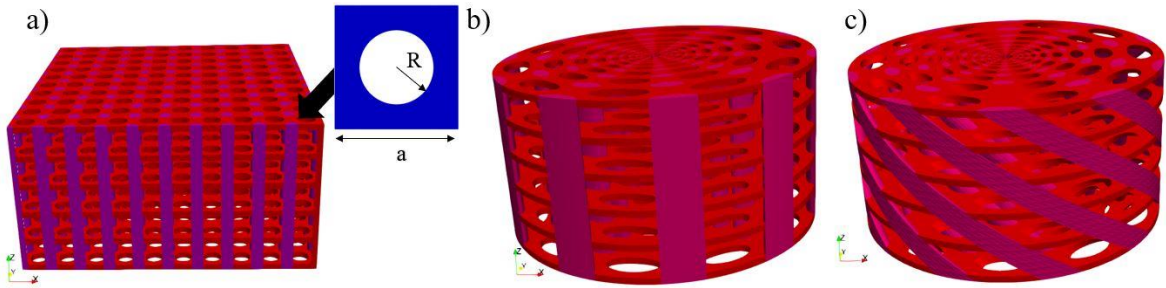


Fig. 3. Mapping of square UC with circular inclusion (SC) with a given porosity of 74 % a) Periodic transformation SC-PT, b) Circular transformation with vertical linking elements SC-CT, c) Circular transformation with inclined linking elements SC-HCT

2.2. SLA fabrication of the design scaffolds

The feasibility of scaffold manufacturing through SLA technique was investigated using a standard setup. Three samples of HC-HCT scaffolds were then fabricated using a Form2 desktop printer (Formlabs Inc, Somerville, MA, USA) and the CLEAR FLGPCL04 resin (Formlabs Inc, Somerville, MA, USA) was used as a constitutive material. The scaffold was printed with a layer height of 25 μm . The HC-HCT configuration was selected since it exhibits the finest geometry at the level of the junctions between UC among the selected subset of scaffold configurations, and because of the expected coupling between compression and torsion modes due to the helical shape of the scaffold. In order to compare the obtained structures with the geometries issued from CAD, μCT acquisition of the three HC-HCT scaffolds were performed using a DeskTom 150 (RX-solutions, Chavanod, France) with a voxel size resolution of 10 μm , a tube voltage of 60 kV, a current of 166 μA and a scanning of 1440 captured pictures. The external geometry was then extracted from thresholding the μCT volume, and the printed support was removed using standard Boolean operations and mesh correction. Geometries extracted from μCT were compared to the initial geometry issued from CAD by computing point-to-surface distances as described in (Chauvelot et al., 2020), based on the Python library PyVista. Using the

CAD geometry as a reference, the two surface meshes were initially put in the same reference frame so as to minimize the mean point-to-surface distance between both geometries, and point-to-surface distances were then calculated and mapped onto the reference CAD geometry.

2.3. Effective mechanical properties of 3D porous scaffolds

The analysis of the effective mechanical properties of the resulting structures was done by seeking the continuous homogeneous medium (*i.e.* endowed with homogenized properties) showing the same behavior as the heterogeneous architected scaffold in the sense of elastic energy storage. In the classical first-gradient theory of elasticity, the Cauchy stress tensor $\boldsymbol{\sigma}$ is related to the infinitesimal deformation $\boldsymbol{\varepsilon}$ (expressed as the symmetrical part of the displacement gradient) through the fourth-order stiffness tensor C_{ijkl} expressed as:

$$\sigma_{ij} = C_{ijkl} \varepsilon_{kl} \quad \text{with} \quad \varepsilon_{ij} = \frac{1}{2} \left(\frac{\partial u_i}{\partial x_j} + \frac{\partial u_j}{\partial x_i} \right) = \varepsilon_{ji} \quad (1)$$

Depending on the transformation used for the design of scaffolds (PT or CT), Cartesian or cylindrical coordinates were more suited to write the above relations. The kinematic variables to be considered within the linear elasticity theory were the six independent strain components ε_{ij} , expressed in Cartesian or cylindrical coordinates. In the current contribution, the attention was drawn on the longitudinal and transverse properties, *i.e.* the scaffold was considered from a structural point of view and modeled as a transversely isotropic material. The apparent elastic properties were calculated using the strain energy based-method (Mindlin, 1964), based on the established relationship between the strain energy of the structure and that of the homogenized equivalent model under specific boundary conditions. The technique has been largely described elsewhere (Cheikho et al., 2022; Goda and Ganghoffer, 2015) and consists in applying elementary kinematic loadings to the structure using a Finite Element (FE) analysis, in order to compute the resulting total elastic Strain Energy (SE) and to determine the components of the overall homogenized stiffness tensor expressed in (2). The studied structures were therefore numerically subject to various macro-strain (denoted E_{ij}), limited to loading cases in the current work, and the total SE stored in the structure under the prescribed Boundary Conditions (BC) was computed using the Abaqus solver (Dassault Systèmes Simulia, United States) after discretization of the structure into C3D4H first-order tetrahedral elements. This total SE was then considered equal to the SE stored in the equivalent homogeneous elastic continuum under the same kinematic loading E_{ii} , in such a way that:

$$U = \frac{V}{2} E_{ij} C_{ijkl} E_{kl} \quad (2)$$

where V represents the volume of the equivalent homogeneous medium, computed from the external contour of the 3D scaffold. The left-hand member U represents the FE-computed elastic SE stored in the structure while the right-hand member is the SE of the equivalent homogeneous continuous medium which is a function of the imposed macro-strain E_{ij} . The transverse compressive modulus E_t was defined as the compressive modulus in response to transverse loads applied in both transverse directions in the case of Cartesian coordinates (PT mapping) or in response to radial loads in the case of cylindrical coordinates (CT mapping). It was identified from the apparent compliance tensor using the relation $E_t = 1/S_{iikk}$ ($i, k = 1, 2$) in Cartesian coordinates (respectively $E_t = 1/S_{rrrr}$ in cylindrical coordinates) where $\mathbf{S} = \mathbf{C}^{-1}$ (Karathanasopoulos et al., 2018) while the longitudinal compressive modulus (E_l) was identified using the relation $E_l = 1/S_{3333}$ (respectively $E_l = 1/S_{zzzz}$ in cylindrical coordinates). The applied boundary conditions are illustrated in Table 1 for both periodic and quasi-periodic cases. Code in the simulations results corresponds to the normalized amplitude of displacement field.

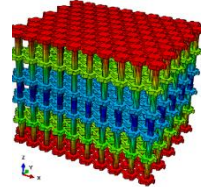
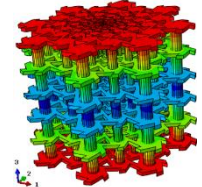
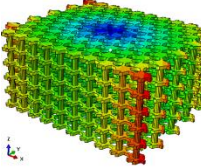
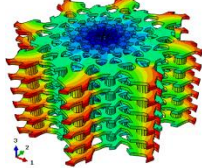
	Periodic structures (Cartesian coordinates)		Quasi-periodic structures (cylindrical coordinates)	
Longitudinal elastic properties E_l		$u_x = 0$ $u_y = 0$ $u_z = z$		$u_r = 0$ $u_\theta = 0$ $u_z = z$
Transverse elastic properties E_t		$u_1 = x$ $u_2 = y$ $u_3 = 0$		$u_r = r$ $u_\theta = 0$ $u_z = 0$

Table 1: Summary of prescribed boundary conditions to identify longitudinal and transverse compressive moduli. PT and CT are used as illustrative examples, and the color code corresponds to the magnitude of the computed displacement field.

In the numerical results exposed hereafter, the elastic properties of CLEAR FLGPCL04 resin given by the manufacturer were selected ($E = 1600$ MPa, $\nu = 0.3$).

2.4. Effect of design variables on the effective mechanical properties

At the end of the design procedure described above, the scaffold structure depends on a set of design variables whose effect on the effective mechanical properties may be computed from the previously detailed method. These mechanical effective properties strongly depended on the UC used in the generation of the 3D scaffold. In our last work (Cheikho et al., 2022), we compared 6 unit cells to illustrate the large range of reachable cross-sectional properties, in order to generate scaffolds that can mimic as close as possible the original mechanical physiological functions of the bone tissue it aims to replace. As stated above, HC and SC cells were used in the present work for illustrative purpose, since they were associated with the maximal and minimal computed transverse cross-sectional compressibility in our former study. Fig. 2 and Fig. 3 illustrate the scaffolds resulting from HC and SC respectively, for PT, CT and HCT transformations, with the same porosity of 74 %. Design variables included the number of UC included in the CT and PT mappings, the layer thickness based on the 2D cross-section, as well as the section, length and inclination of linking elements. A full-size sensitivity analysis of each of these design variables on each of the components of stiffness tensor was considered out of the scope of the present contribution. Alternatively, we selected a subset of relevant effective properties for an application in scaffold selection for bone repair such as the longitudinal and transverse compressive moduli (in order to highlight the anisotropy of the resulting structures).

Since the porosity of the scaffold plays a critical role in its capacity to be colonized by tissue growth (Bandyopadhyay et al., 2010; Torres-Sanchez et al., 2017), the effect of various porosities on the obtained effective mechanical properties was first assessed. From the design procedure described above, a simple way to control the overall scaffold porosity was to affect the porosity of the single UC, as done previously (Cheikho et al., 2022), and as illustrated in Fig. 4. An alternative or additional way to control overall scaffold porosity was to change the diameter of linking elements between two layers, as illustrated in Fig. 5.

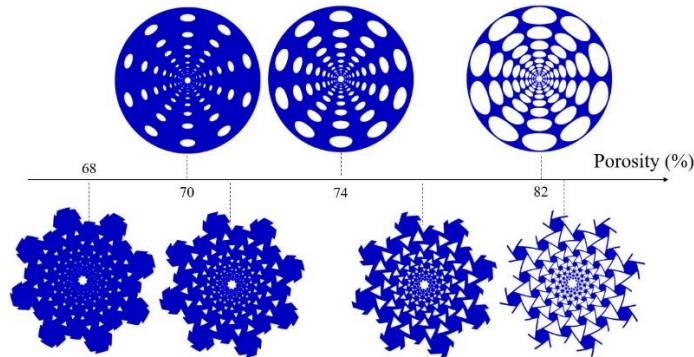


Fig. 4. Cross-sections geometries with SC and HC unit cells for different porosities, based on the variation of pore size in the initial UC.

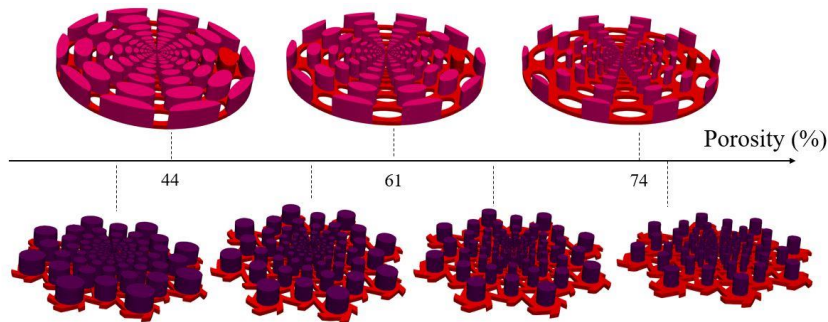


Fig. 5. Cross-sections geometries with SC and HC unit cells for different porosities, based on the variation of the diameter of linking elements between two layers.

In order to modify the overall geometry, and for a fixed porosity, the combination of the two aforementioned design variables also permitted to generate various scaffold designs by varying in parallel the pore size in the UC and the section of linking elements. Fig. 6 offers an example of the obtained geometries with a fixed porosity of 74% but by different combinations of these parameters. This additional design variable was quantified by computing the ratio between the volume of a layer and the total volume of the scaffold, and its effect on effective mechanical properties of the scaffold was also assessed.

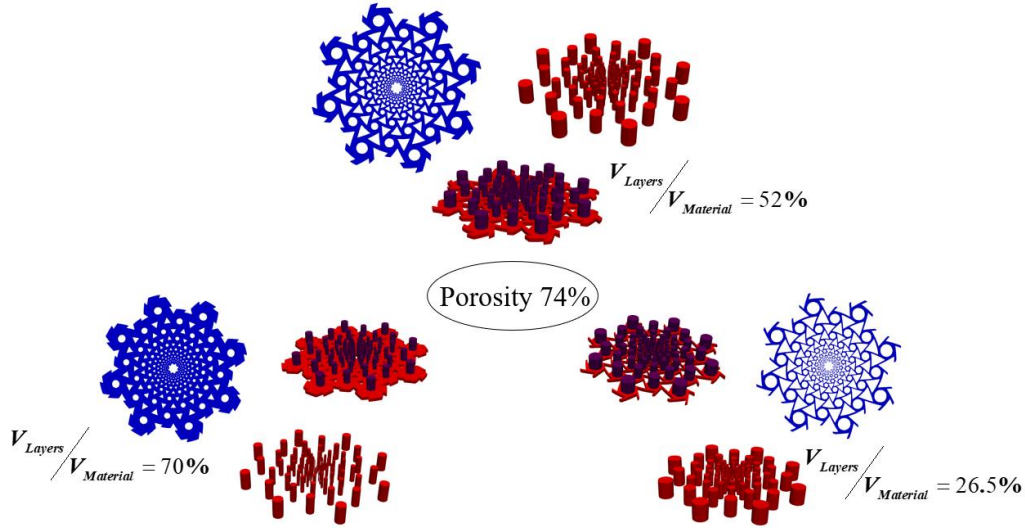


Fig. 6. Geometry of an elementary stack within the scaffold with HC unit cell for a fixed overall porosity $P = 74\%$, based on the variation of the ratio between the layer volume and the overall volume of the scaffold.

Lastly, in the case of HCT configuration, the angle of inclination of the linking elements was expected to strongly affect the longitudinal compressive modulus of the scaffold. The effect of this last design variable was also studied in order to emphasize the possibility to control scaffold anisotropy by varying the total angle of rotation of the helical scaffold.

2.5. Mechanical testing and confrontation with numerical results

A preliminary mechanical characterization was performed in order to confront the obtained numerical results with experimental data and investigate the validity of our approach. The HC-HCT configuration was selected to evaluate our numerical procedure in the worst case, since its effective properties were expected to critically depend on the strain concentration in some fine parts of the geometry that may be difficult to fabricate. The three HC-HCT scaffolds obtained by SLA were thus tested using a Zwicki Z0.50 TN equipped with a 100 N load cell, by simply positioning the samples between two compression plates. A longitudinal compression test was firstly performed up to 80 N to avoid structural damage. Due to chiral effects induced by the helical shape of the HC-HCT scaffold, coupling between compression and torsion modes were expected (Meng et al., 2020; Xin et al., 2020), and they were only restrained by the friction between the sample and the compression plates. Since the transverse compression test simulated in our previous work (Cheikho et al., 2022) was practically very difficult to achieve, a transverse compression test (also known as brazilian test in geomechanics) was performed in order to confront our numerical predictions with experimental data in the transverse direction. The tests were performed on the same sample to gather as many data as possible and the last transverse test was performed up to the collapse of the structure.

Force-displacement curves were then extracted and compared to the numerical results obtained from the CAD geometry. Concerning longitudinal compression tests, two types of BC were considered in the numerical model in order to consider the coupling effect between compression and torsion, partially restrained by the friction between compression plate and the sample. In the first case (named *free BC* hereafter), the upper boundary of the scaffold was considered totally free, corresponding to a perfect sliding, while in the second

case (named *fixed BC* hereafter) it was considered fixed corresponding to a perfect sticking between plate and sample. In parallel, in order to investigate the capacity of our numerical approach to fit experimental data when the exact geometry was considered, the same two mechanical tests were simulated taking the μ CT geometry as an input of the FE procedure instead of the CAD geometry. Videos (available upon request) were recorded using a high-resolution camera (AVT Manta 12 Mpx) to precisely monitor the kinematics of scaffold compression.

3. Results

3.1. Effective mechanical properties of 3D porous scaffolds

The six scaffolds illustrated previously in Fig.2 and Fig. 3, designed with a fixed porosity of 74 %, were considered in this study in order to investigate the effect of the selected UC and stacking procedure on the computed effective properties. As expected, we observed that the four scaffold configurations SC-PT, SC-CT, HC-PT and HC-CT exhibited an identical effective longitudinal compressive modulus of $E_l = 218$ MPa since this value results from the contribution of longitudinal linking elements, that were identical in each of these configurations. Structures based on HC exhibited lower transverse compressive modulus than the structures generated from the SC, as emphasized previously. The ratio between the transverse compressive modulus in periodic configurations SC-PT and HC-PT was $E_{t\text{ SC-PT}}/E_{t\text{ HC-PT}} = 2.65$, while it was higher in graded configurations SC-CT and HC-CT, namely $E_{t\text{ SC-CT}}/E_{t\text{ HC-CT}} = 3.25$, indicating that the CT mapping accentuated the contrast between the selected UC. In the case of helical configurations (SC-HCT and HC-HCT) with a total twist of $\alpha = \pi/2$ through the whole scaffold, the effective longitudinal compressive modulus of $E_l = 58$ MPa was considerably lower than for longitudinal linking elements with a constant observed ratio of $E_{l\text{ SC-PT}}/E_{l\text{ SC-HCT}} = E_{l\text{ HC-PT}}/E_{l\text{ HC-HCT}} = 3.7$. This indicated that the inclination of linking elements permitted to control the longitudinal stiffness of the designed scaffold, and therefore its anisotropy, depending on the selected angle. By comparing the transverse compressive modulus of the scaffolds generated with the periodic transformation and the ones generated with the circular transformations ($E_{t\text{ SC-PT}} = 132$ MPa \rightarrow $E_{t\text{ SC-CT}} = 123$ MPa) and ($E_{t\text{ HC-PT}} = 50$ MPa \rightarrow $E_{t\text{ HC-CT}} = 49$ MPa), we observed that graded scaffolds were associated with a weaker transverse compressive modulus compared to periodic scaffolds. The Poisson's coefficients of these structures between the transverse and longitudinal directions vary in the range of $\nu_{tl} \in [0, 0.6]$. The value $\nu_{tl} = 0$ obtained for some configurations corresponded to a total separation between longitudinal and transverse properties, while the highest Poisson's ratio obtained for SC-HCT indicated a strong coupling between longitudinal and transverse properties.

3.2. Effect of design variables on the effective compressive moduli

The effect of the subset of design variables illustrated in Fig. 5, Fig. 6 and Table 1 were investigated. Fig. 7 illustrates the influence of porosity on the computed effective compressive moduli (transverse and longitudinal) of the scaffold, when the porosity of the UC was taken as a design variable (as illustrated in Fig. 5). For a given porosity, the HC-based structures showed less stiff mechanical properties than SC-based structures. However, similar properties were obtained for low porosities, since the auxetic effect governed by the fineness of the HC cell vanished in the case of a more massive UC. As expected, the longitudinal compressive modulus was not affected by a change of UC porosity in the case of PT and CT mappings. However, this did not hold true for helical scaffolds, with a monotonically decreasing longitudinal compressive modulus as the porosity increased, indicating strong couplings between the cross-sectional properties of the scaffold layers and its longitudinal behavior.

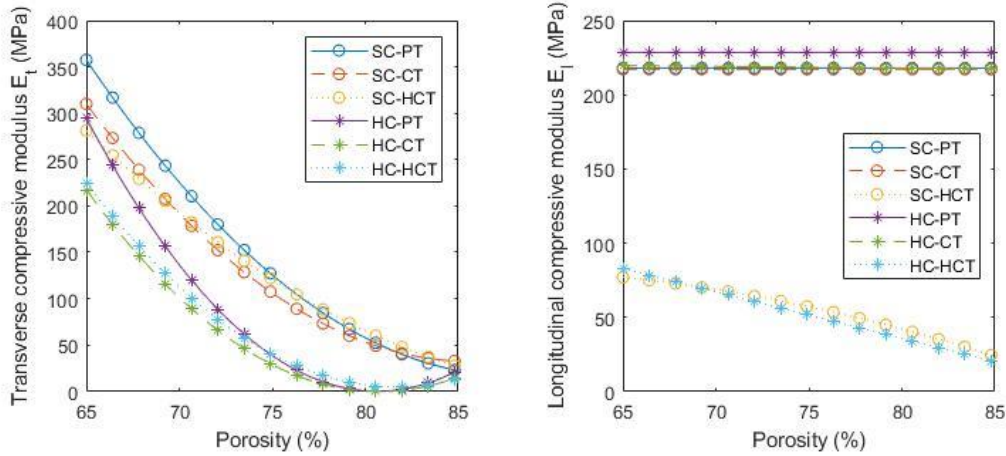


Fig. 7. Transversal and longitudinal compressive moduli as a function of porosity, based on the variation of pore size in the UC.

Fig. 8 illustrates the influence of porosity on the computed effective compressive moduli of the scaffold, when the diameter of linking elements between two layers was taken as a design variable (as illustrated in Fig. 6). The goal was then to adjust the effective mechanical properties of the scaffold for a given choice of the cross-section. In contrast to previous results which only affected the transverse properties, changing the diameter of linking elements had an effect on the apparent mechanical properties in both transverse and longitudinal directions. Non-surprisingly, the longitudinal compressive modulus linearly decreased with increasing porosity for PT and CT scaffolds, while this relation was not linear in HCT scaffolds due to couplings. A linear relation was also observed between the porosity and the transverse properties for HC-based scaffolds exclusively.

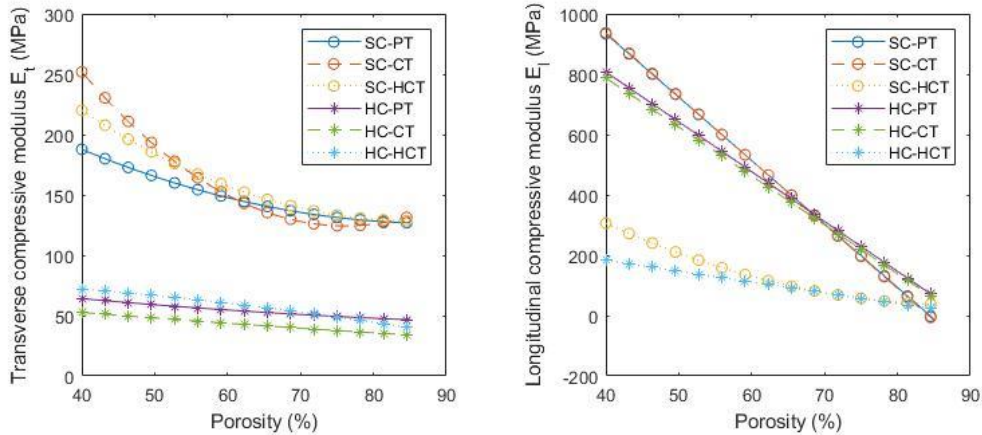


Fig. 8. Transversal and longitudinal compressive moduli as a function of porosity, based on the variation of the diameter of linking elements between two layers.

Fig. 9 illustrates how the combination of these two design variables may permit to obtain different effective mechanical properties for a given overall porosity. The effect of the ratio between the volume of a layer and the total volume of the scaffold on its effective compressive moduli was investigated, which permitted to cover a large range of reachable properties. We found that for a minimum volume of material in the layers, which corresponds to a maximum size of the inclusions in the cross-section with a maximum diameter of linking elements, the transverse compressive modulus was minimal and the longitudinal compressive modulus exhibited maximum values. As the volume of material in the layers increased, the radius of the inclusion decreases, resulting in an increased diameter of linking elements, and therefore in an increase of transverse stiffness and a decrease in longitudinal stiffness.

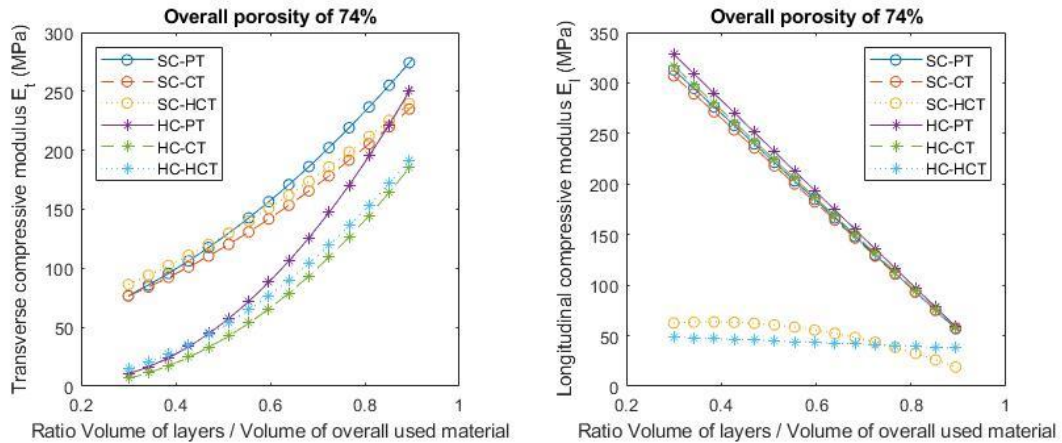


Fig. 9. Transversal and axial compressive moduli for a fixed porosity of 74 % when varying the ratio of the layer's volume in function to the total volume of material.

Among the different design variables that may affect the effective properties of the scaffold, and apart from the overall porosity, the effect of the helical shape of the scaffold resulting from the inclination of linking elements was also assessed. This effect was quantified through the total twist angle α , *i.e.* the total relative angle α between the first and the last layer of the structure, ranging between $\alpha = 0$ and $\alpha = \pi/2$. Results are illustrated in Fig. 10 for structures based on SC and HC. This angle was observed to drastically affect the longitudinal compressive modulus for both structures (by a factor of 5), while it poorly affected transverse properties.

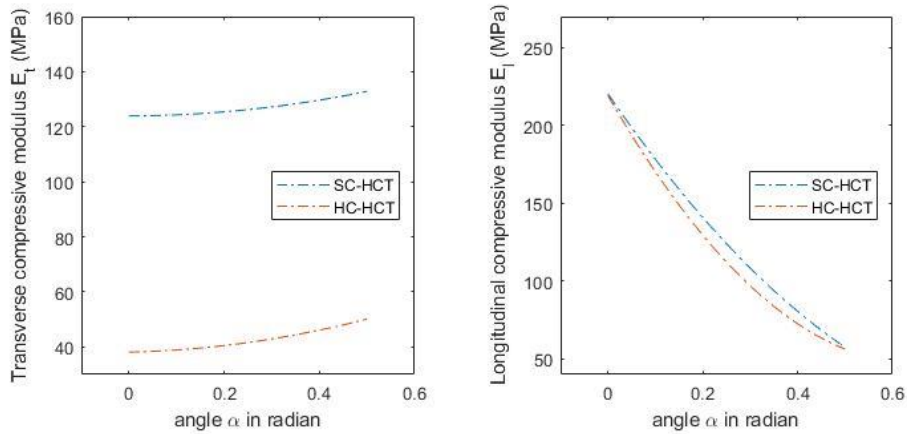


Fig. 10. Transversal and longitudinal compressive moduli as a function of the total twist rotation angle α .

A more exhaustive parametric study was conducted by considering the SC and the HC unit cells generated with the three transformations PT, CT and HCT. The results of the parametric study in terms of transverse and longitudinal compressive moduli are illustrated in a scatter plot in Fig.11 from overall porosity going from 50 % to 85 %, These results indicate a strong anisotropy for some of the tested configurations, and ratios up to 6 between transverse and longitudinal compressive moduli for the configuration HCN-HCT.

3.3. Manufacturability of the proposed 3D porous scaffolds

The capacity to obtain the designed scaffolds from SLA fabrication was assessed for a HC-HCT graded scaffold with a given porosity of 68 %, as illustrated in Fig. 4. The selected structure was based on the repetition of 6 layers in order to form a scaffold of 5.2 mm in height and 10mm in diameter, as observed in Fig. 12.

Substantial differences between CAD geometry and obtained scaffold were observed at the center of the graded structure, where pore sizes were minimal and lower than the resolution capabilities of the SLA equipment. Such differences were quantified by computing the point-to-surface distances between the geometries issued from CAD and μ CT, as illustrated in Fig. 13, taking CAD geometry as a reference. The distance map highlighted the differences between designed and printed geometries at the center of the scaffold, with distances higher than 1mm, while the overall geometry of the scaffold was satisfyingly obtained.

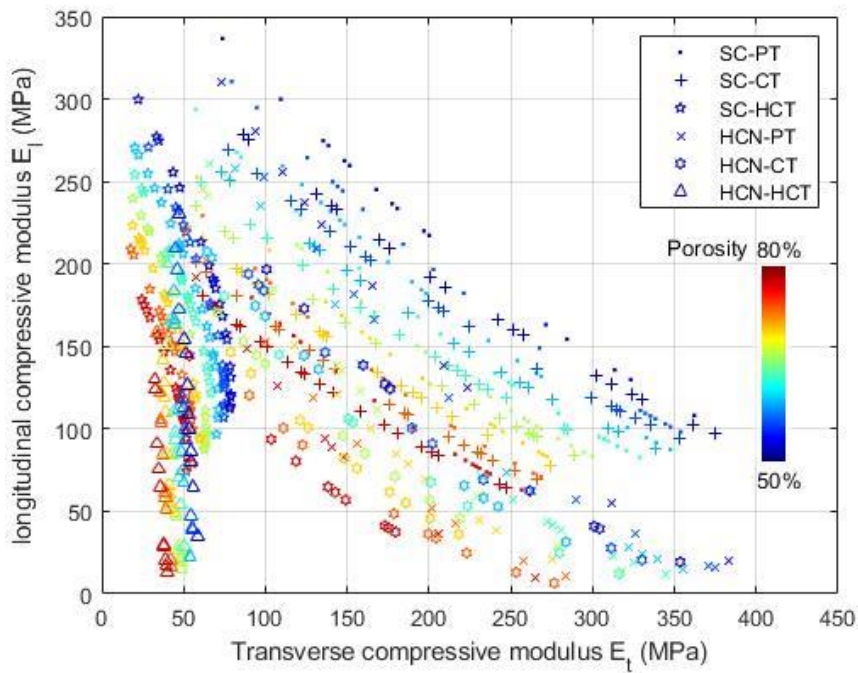


Fig. 11. Transversal and longitudinal compressive moduli of the transformations PT, CT and HCT applied on the unit cells SC, HC. The colors characterize the overall porosity of the resulting structure. The marker symbols characterize the corresponding scaffold architecture.

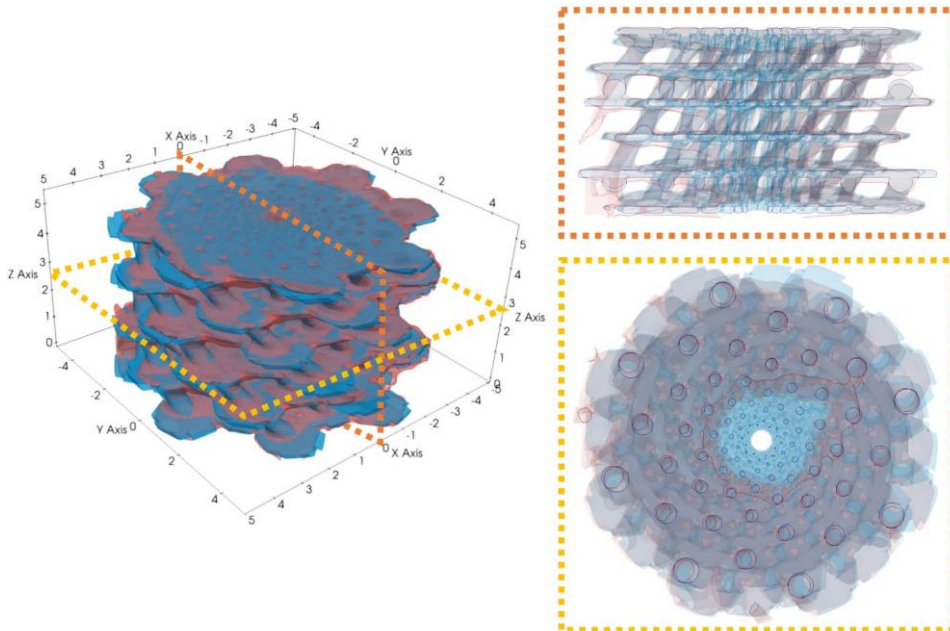


Fig. 12. (left) Superposition of the CAD or target (blue) and μ CT or real (orange) geometries. (right) Longitudinal and transverse cross-sections, highlighting the scaffold contours of CAD and μ CT geometries.

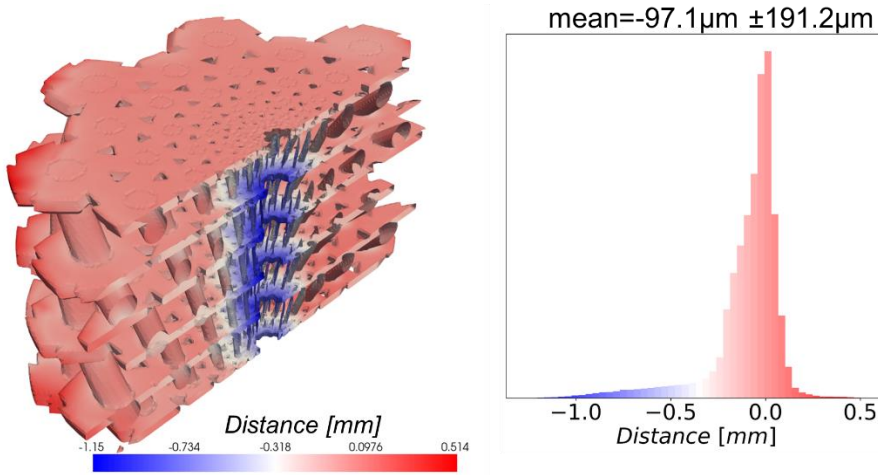


Fig. 13. Point-to-surface distances between geometries issued from CAD and μ CT

3.4. Mechanical testing and confrontation with numerical results

Mechanical tests were performed on three different HC-HCT scaffolds in order to evaluate the predictive capacity of our numerical approach. Representative images of the initial and deformed configurations of scaffolds after the longitudinal and transverse compression test are represented in Fig. 14.

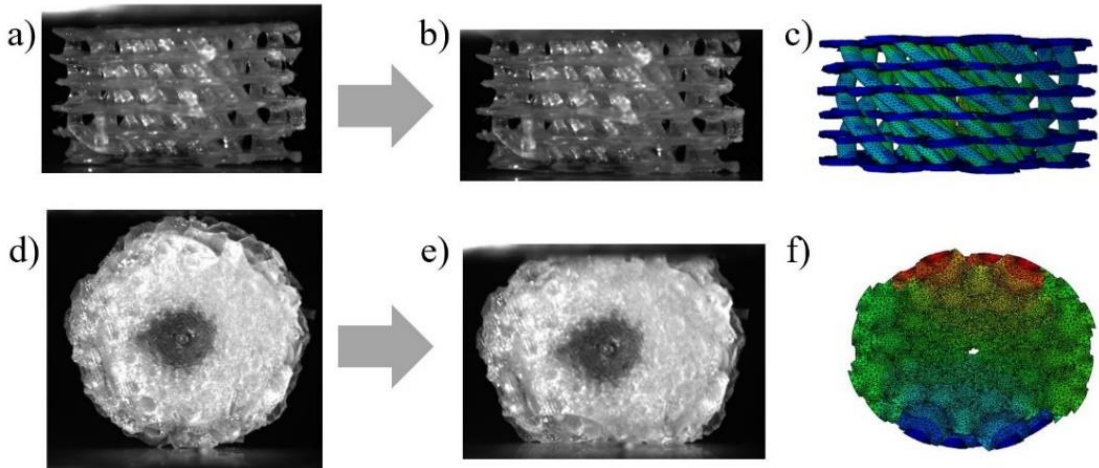


Fig. 14. Compression test and Brazilian test. a, d) Initial configuration of HC-HCT scaffolds in longitudinal and transverse positions. b, e) Final configuration after the prescribed load. c, f) Corresponding numerical simulations after the prescribed load. The color code stands for the magnitude of the displacement field.

Corresponding FE simulations were performed for both longitudinal (Fig. 14.c) and transverse compression tests (Fig. 14. f), and results were compared to experimental data in terms of force-displacement responses. In a first case, the CAD geometry was considered as an input of the FE procedure (named FE-CAD hereafter), while in a second case, the reconstruction issued from μ CT segmentations were used as in input (named FE- μ CT hereafter), including the artefacts due to the fabrication as detailed in the previous section. Moreover, in the case of longitudinal compression test and due to coupling effects, two types of BC's were considered corresponding to free BC or fixed BC at the level of the upper compression plate, since the actual friction interaction probably lied between these two extreme BC's. Experimental and numerical FE results are illustrated in Fig. 15.

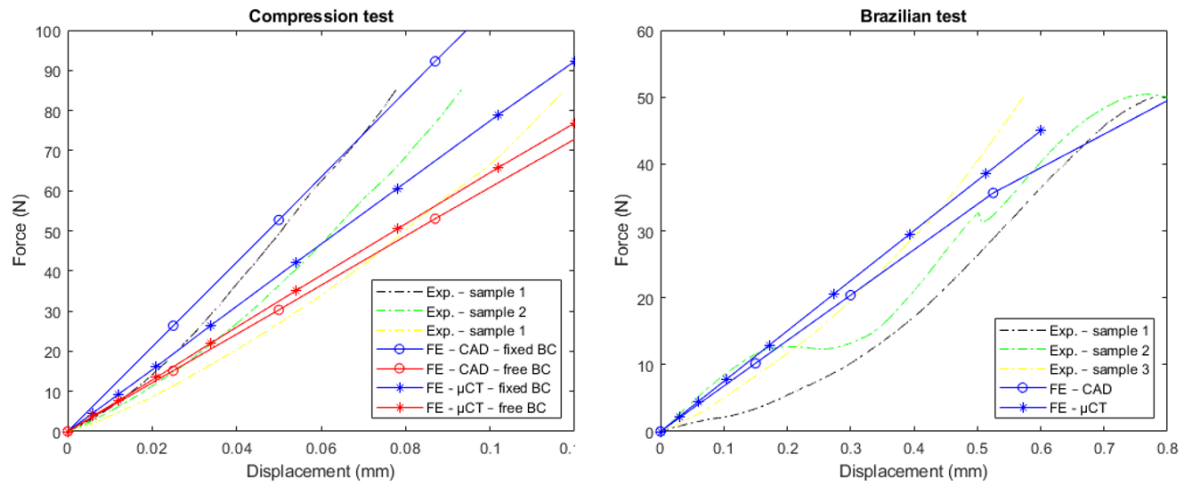


Fig. 15. Experimental and numerical results of the longitudinal compression test and Brazilian test. Numerical results were obtained considering both CAD and μ CT geometries as an input.

In the case of the longitudinal compression test, it was observed that the three experimental tests were associated to a large variability of responses, as illustrated in Fig. 15. Such a variability may be attributed to the fabrication artefacts, since the overall behavior of the scaffolds strongly depended on the fineness of the architecture which may not be accurately reproduced after SLA fabrication. This may also be attributed to the friction interaction between the plate and sample that may depend on the upper surface smoothness. It is noticeable that no obvious damage appeared on the compression force displacement curves. Despite this variability, experimental data were consistent with the numerical response, and lied perfectly between the two boundary cases consisting in free-BC and fixed-BC, indicating that the actual friction interaction between the compression plate and the sample lied between situations of perfect sliding and sticking contact. As far as transverse compression was concerned (brazilian test), the experimental data revealed non-linear responses or non-monotonic responses. From the analysis of recorded videos, this was due to the growing contact between the compression plate and the heterogeneous scaffolds structure, progressively inducing local damage at the level of the fine UC structure, and distributing the load over an increasing region of the scaffold. This phenomenon was not considered in FE simulations, since a macro-strain was applied by prescribing a displacement to scaffold boundary without explicitly modeling the contact with the compression plate. However, the computed responses were in good accordance with experimental data despite the geometrical artefacts highlighted previously.

4. Discussion and conclusion

Numerous studies have been devoted to the design of porous scaffolds for bone repair over the past two decades. The advances in the field of design strategies for the development of scaffolds and devices with tailored morphology and integrated functionalities are crucial because they aim to improve patient outcomes, reduce complications, improve the quality of life for individuals with missing or damaged body parts, address unmet medical needs, and drive technological innovation. By developing a flexible design framework to design scaffolds, the long-term objective of the present approach is to provide better support for tissue growth and repair, or more closely mimic the form and function of a missing or damaged body part. The identification of the most suitable porous structure for a given clinical application still remains a challenge, since the key requirements involve both morphological considerations such as porosity and mechanical effective properties such as compressive modulus or anisotropy (Rüegg et al., 2017). These two parameters are obviously strongly related for cellular structures (Gibson, 2005), and the influence of scaffold porosity on its effective mechanical properties has been widely reported (Bandyopadhyay et al., 2010; Karageorgiou and Kaplan, 2005; Poh et al., 2019). These interrelated requirements justify the need to propose a design framework in which porosity and mechanical properties may be governed by design variables. In the current state of art, most 3D scaffolds are based on the repetition of a UC, and they most often result in isotropic structures with a homogeneous pore distribution. On the contrary, the initial bone tissue is far from isotropic (Li et al., 2013). In addition, there is a growing interest in designing scaffolds that exhibit a pore size gradient. In response to these needs, the first objective of the present contribution was to propose a design procedure in which graded scaffolds may be obtained, with tunable and anisotropic mechanical properties, as an extension of a recently proposed framework to design graded cross-sections (Cheikho et al., 2022). This former 2D design procedure was therefore extended to generate various 3D scaffold structures, by simply stacking layers of graded cross-sections through the creation of longitudinal linking elements between these layers. In order to restrict the large range of structures that may be obtained, we selected two types of UC's (SC and HC) based on the resulting computed properties reported previously, for which we selected two types of mappings (PT and CT) which permitted to form periodic and cylindrical graded scaffolds respectively. The reported methodology largely overcomes some of the limitations of reported studies focusing on graded scaffolds : indeed, graded structures in the literature are often based on linear gradients of porosities (Afshar et al., 2016; Liu et al., 2018; Zhou et al., 2020), while pore size gradient from the core to the periphery has been proved to be preferable (Ahn et al., 2010). In the few studies reporting radial pore size gradients in cylindrical structures (Liao et al., 2021a; Limmahakhun et al., 2017a), gradients have been obtained through radially distributing a parameter of the UC which limits the reachable pore size to the UC size. In the present procedure, very large pore size gradients from the core to the periphery of 3D cylindrical scaffold can be obtained by making use of circular mapping issued from conformal transformations, mimicking natural architectures such as sunflowers that are widely used in other fields of physics (Drenckhan et al., 2004).

The numerical method reported formerly for 2D sections was extended to 3D scaffolds in order to evaluate the equivalent structure-level effective elastic properties. This method implemented in Abaqus and based on our team's work in periodic homogenization (Goda et al., 2016; Goda and Ganghoffer, 2015) permitted to efficiently predict the effective scaffold properties for a given scaffold configuration. It permitted the determination of each and every components of the stiffness tensor \mathbf{C}_{ijkl} of the homogenized continuum structure, by prescribing different kinematic loadings which separately activated each of the elastic properties. However, for the sake of conciseness and clarity, and contrary to former studies (Goda and Ganghoffer, 2015), we did not exhaustively discuss each component of \mathbf{C} and restricted our results to some of the relevant effective mechanical properties of the scaffold. This method enabled to analyze the relations between porosity and effective mechanical properties of the scaffold. Porosity was governed by different design variables such as the

pore size in UC or the diameter of linking elements. It was found that pore size in the UC strongly impacted the transverse compressive modulus and slightly affected the longitudinal compressive modulus, while the opposite was true for the diameter of linking elements. Combined together, the two design variables also allowed to reach a wide range of effective properties for a given porosity, fixed at 74% as an example is the present work. We demonstrated the strong influence of this combination of variables, quantified through the ratio between volume layer and overall volume of the material, on both the transverse and longitudinal properties. As expected, effective longitudinal compressive modulus simply resulted from the sum of the contribution of these linking elements in the case of a simple stacking of layers with vertical elements. In order to widen the range of reachable effective properties and decrease the resulting longitudinal properties if the application requires to do so, we pointed out that an overall twist angle in the stack of layers substantially decreased the resulting longitudinal properties. In that way, during the design procedure, the stiffness in the longitudinal direction can be selected (in the range of reachable properties for a given constitutive material) independently from the transverse stiffness. This transverse stiffness can be furtherly selected by choosing the appropriate UC, mapping and porosity, in order to obtain the target properties. It is worthy to emphasize that the computed apparent properties for the different configurations are far lower than initial bone properties, due to the low elastic properties of the constitutive resin of the scaffold considered in the present study. This has led different authors to prefer scaffold based on metallic powders (Liao et al., 2021a; Rüegg et al., 2017), while the present approach concerns regenerative medicine which requires biodegradable polymeric materials (Peltola et al., 2008; Wang et al., 2020; Weisgrab et al., 2020).

From the present results, the separated selection of longitudinal and transverse properties may find many applications for minimally invasive surgery applications (Bobbert et al., 2020; Di et al., 2016; Langford et al., 2021; Senatov et al., 2017), so that the proposed self-fitting scaffolds may be easily manually (or instrumentally) compacted in the transverse directions to pass through a bone tunnel whose radial dimensions are smaller than the final expanded scaffold geometry. This opens up many clinical possibilities in dentistry (Di et al., 2016) or for the repair of cranial vault defects (Berner et al., 2014; Lance and Wong, 2016). To furtherly study large deployable configurations, the assumption of small strains in the framework of linear elasticity should be however overcome by extending the proposed approach to large deformations, including buckling instabilities (Linn and Oliveira, 2017) that could appear locally in fine parts of the scaffold microstructure, which constitutes one of the major perspectives of the present study.

The practical relevance of such an engineering process may be obviously limited by technical issues, since the resulting structures may not be compatible with their fabrication using standard additive manufacturing techniques. In order to investigate such limitations, the manufacturability of the proposed scaffold by SLA was studied by analyzing the discrepancies between the CAD-based geometry and the actual obtained geometry after manufacturing. A single HC-HCT scaffold configuration was selected, since it constituted the most challenging case with the finest microstructural parts at the center of the scaffold due to circular mapping, and since it was expected to exhibit compression-torsion coupling in further mechanical characterization. The actual microstructure issued from the segmentation of μ CT was compared to CAD geometry, and errors superior to 1mm (for a scaffold diameter of 10mm) were observed at the center of the scaffolds. This indicated that the fine microstructure of HC-HCT was badly reproduced by the SLA process in the core of the structure due to the very fine pore size in this area. In order to tackle this limitation, it is envisaged in further studies to design tubular scaffold with a clear cylindrical space at the level of the scaffold core, since the low pore size in the central area of the scaffold lied anyway out of the suitable pore size range for bone ingrowth (Oh et al., 2007; Torres-Sanchez et al., 2017). Moreover, this tubular space may encourage the vascularization of the bone scaffold through the apparition of central blood capillaries (He et al., 2013). Alternatively, in order to more accurately reproduce the fine scaffold microstructure, other submicron additive manufacturing techniques (Bückmann et al., 2014; Weisgrab et al., 2020) may be considered. However, such expensive and time-

consuming processing techniques may restrict their clinical relevance, since the cost of the proposed bone substitute constitutes a critical milestone to reach the clinical daily practice.

These discrepancies at the center of some of the scaffold configurations due to SLA manufacturing may obviously impair the conclusions of the mechanical simulations detailed in the present contribution. In order to investigate the predictive capacity of our numerical results, a preliminary mechanical characterization was performed on three samples of HC-HCT scaffolds. Longitudinal and transverse tests were done on the same sample, assuming that the longitudinal test did not include any damage in the scaffolds. Transverse tests were performed up to structure collapse, and damage was clearly observed locally at the level of the interface between the sample and the compression plate. The imperfections in SLA printing were associated to a high variability between samples. Due to the chiral geometry of the HC-HCT scaffold, compression-torsion couplings effect was observed as reported in the literature (Meng et al., 2020; Xin et al., 2020). This coupling was however restrained by the friction interaction between the sample and the compression plate, while an *ad hoc* set up with a free rotation at the level of the upper compression plate may have been suited, as generally reported for the accurate characterization of coupling effects in metamaterials (Durand et al., 2022). These preliminary experiments permitted however to verify the good accordance between our numerical FE predictions and experimental data. The coupling effect was emphasized by the difference between free and fixed BC's applied in the FE model. While the contrast between these two types of BC was strong in the case of CAD-based meshes, it was less pronounced for μ CT-based meshes, indicating that the fabrication artefacts may decrease the coupling effect between torsion and compression by inaccurately reproducing the helical structure of the scaffold. This preliminary experimental study, despite the limited number of associated samples and scaffold configurations, permitted to verify the good accordance between numerical and observed effective properties, and suggested that the reported predicted mechanical properties were reliable despite fabrication artefacts.

As previously mentioned, the challenge addressed in this work was to propose microstructures with architected gradients in pore size. Among the list of required specifications for scaffold design, the permeability of the structure may obviously also be of primary importance since it conditions tissue growth (Dias et al., 2012; Pasha Mahammod et al., 2020). This particular point has motivated the proposition of TPMS scaffolds (Montazerian et al., 2017; Santos et al., 2020), that have proven to be an effective and feasible tool for designing porous and interconnected structures. By affecting UC size in TPMS structures, recent studies have reported graded structures however limited by low porosity contrasts since the size of the pore size gradient cannot exceed the size of the UC. The proposed strategy in the current contribution overcome this limitation by permitting high pore size gradients, that have been showed to improve nutrient diffusion (Ahn et al., 2010). Scaffold permeability is obviously linked with the interconnectivity of the associated pore network (Jones et al., 2009) : in the proposed structures, and due to the stacking of 2D cross-sections, the pore network is fully interconnected. The characterization of the proposed scaffolds permeability depending of UC and conformal mappings using computational fluid dynamic (as proposed for example in (Ali et al., 2020)) could constitute a promising perspective of the present work, in order to help in the selection of the most suited configuration for tissue growth.

As a conclusion, the present contribution reported a versatile framework for anisotropic scaffold design, including periodic or non-periodic graded structures, enabling to separately select the transverse and longitudinal properties and overall porosity. While some of the reported strategies for the design of scaffolds may permit to obtain either pore size gradients, adjustable morphological or mechanical properties, or overall anisotropy, the present contribution permit to simply combine each of these specificities within a single design framework based on conformal mappings. We have shown that design parameters such as the selected UC, conformal mapping, of degree of longitudinal twist permit to finely control the obtained scaffold properties. We have also demonstrated that such properties were predictable from computational simulations with a good level of confidence, thus avoiding the need for a trial-and-error approach in order to select an appropriate scaffold

for a given application. Despite observed differences between the CAD geometry and actual geometry obtained through SLA fabrication, the reported numerical methods permitted to satisfyingly predict the effective mechanical properties for a given scaffold configuration. In the future, a wide variety of scaffold configurations will be generated and confronted from a biological point of view, focusing on their ability to promote bone ingrowth. Promising perspectives are also offered concerning self-fitting deployable scaffolds, providing that the present methodology is extended to large deformation analyses including the tracking of microstructural instabilities. The reported contribution constitute a new strategy to design scaffold geometry and may therefore help to reduce the risk of complications and improve the long-term success of these therapies, resulting in the improvement of the quality of life for individuals with missing or damaged body parts by providing better function, aesthetics, and comfort. In addition, these advances may provide new and improved therapies in case of inadequate actual treatments, and can drive innovation in the fields of tissue engineering and prosthetics by enabling the development of new and improved products and processes.

Acknowledgements

The authors thank the French research agency (ANR) for the financial support provided by the ANR project “ArchiMatHos” devoted to metamaterials, as well as the INSIS-CNRS for their financial support concerning the field of *material by design*. The authors would also like to thank Mr Vincent Marquet for his contribution on CAD models prior to SLA fabrication.

References

- Afshar, M., Anaraki, A.P., Montazerian, H., Kadkhodapour, J., 2016. Additive manufacturing and mechanical characterization of graded porosity scaffolds designed based on triply periodic minimal surface architectures. *Journal of the Mechanical Behavior of Biomedical Materials* 62, 481–494. <https://doi.org/10.1016/j.jmbbm.2016.05.027>
- Ahn, G., Park, J.H., Kang, T., Lee, J.W., Kang, H.-W., Cho, D.-W., 2010. Effect of pore architecture on oxygen diffusion in 3D scaffolds for tissue engineering. *J Biomech Eng* 132, 104506. <https://doi.org/10.1115/1.4002429>
- Andrianov, I.V., Awrejcewicz, J., Diskovsky, A.A., 2006. Homogenization of Quasi-Periodic Structures. *Journal of Vibration and Acoustics* 128, 532–534. <https://doi.org/10.1115/1.2202158>
- Ayad, M., Karathanasopoulos, N., Ganghoffer, J.F., Lakiss, H., 2020. Higher-gradient and micro-inertia contributions on the mechanical response of composite beam structures. *International Journal of Engineering Science* 154, 103318. <https://doi.org/10.1016/j.ijengsci.2020.103318>
- Bahraminasab, M., 2020. Challenges on optimization of 3D-printed bone scaffolds. *BioMedical Engineering OnLine* 19, 69. <https://doi.org/10.1186/s12938-020-00810-2>
- Bandyopadhyay, A., Espana, F., Balla, V.K., Bose, S., Ohgami, Y., Davies, N.M., 2010. Influence of porosity on mechanical properties and in vivo response of Ti6Al4V implants. *Acta Biomaterialia* 6, 1640–1648. <https://doi.org/10.1016/j.actbio.2009.11.011>
- Berner, A., Woodruff, M.A., Lam, C.X.F., Arafat, M.T., Saifzadeh, S., Steck, R., Ren, J., Nerlich, M., Ekaputra, A.K., Gibson, I., Huttmacher, D.W., 2014. Effects of scaffold architecture on cranial bone healing. *Int J Oral Maxillofac Surg* 43, 506–513. <https://doi.org/10.1016/j.ijom.2013.05.008>
- Bobbert, F.S.L., Janbaz, S., van Manen, T., Li, Y., Zadpoor, A.A., 2020. Russian doll deployable meta-implants: Fusion of kirigami, origami, and multi-stability. *Materials & Design* 191, 108624.

<https://doi.org/10.1016/j.matdes.2020.108624>

- Bobbert, F.S.L., Zadpoor, A.A., 2017. Effects of bone substitute architecture and surface properties on cell response, angiogenesis, and structure of new bone. *J. Mater. Chem. B* 5, 6175–6192. <https://doi.org/10.1039/C7TB00741H>
- Brennan, M.A., Davaine, J.-M., Layrolle, P., 2013. Pre-vascularization of bone tissue-engineered constructs. *Stem Cell Res Ther* 4, 96. <https://doi.org/10.1186/scrt307>
- Bückmann, T., Thiel, M., Kadic, M., Schittny, R., Wegener, M., 2014. An elasto-mechanical unfeelability cloak made of pentamode metamaterials. *Nature Communications* 5, 4130. <https://doi.org/10.1038/ncomms5130>
- Chartrain, N.A., Williams, C.B., Whittington, A.R., 2018. A review on fabricating tissue scaffolds using vat photopolymerization. *Acta Biomaterialia* 74, 90–111. <https://doi.org/10.1016/j.actbio.2018.05.010>
- Chauvelot, J., Laurent, C., Le Coz, G., Jehl, J.-P., Tran, N., Szczetynska, M., Moufki, A., Bonnet, A.-S., Parietti-Winkler, C., 2020. Morphological validation of a novel bi-material 3D-printed model of temporal bone for middle ear surgery education. *Ann Transl Med* 8. <https://doi.org/10.21037/atm.2020.03.14>
- Cheikho, K., Laurent, C., Ganghoffer, J.F., 2022. An advanced method to design graded cylindrical scaffolds with versatile effective cross-sectional mechanical properties. *Journal of the Mechanical Behavior of Biomedical Materials* 125, 104887. <https://doi.org/10.1016/j.jmbbm.2021.104887>
- Deng, F., Liu, L., Li, Z., Liu, J., 2021. 3D printed Ti6Al4V bone scaffolds with different pore structure effects on bone ingrowth. *Journal of Biological Engineering* 15, 4. <https://doi.org/10.1186/s13036-021-00255-8>
- Di, S., Liu, X., Liu, D., Gong, T., Lu, L., Zhou, S., 2016. A multifunctional porous scaffold with capacities of minimally invasive implantation, self-fitting and drug delivery. *Materials Today Chemistry* 1–2, 52–62. <https://doi.org/10.1016/j.mtchem.2016.11.004>
- Dias, M.R., Fernandes, P.R., Guedes, J.M., Hollister, S.J., 2012. Permeability analysis of scaffolds for bone tissue engineering. *Journal of Biomechanics* 45, 938–944. <https://doi.org/10.1016/j.jbiomech.2012.01.019>
- Donate, R., Monzón, M., Alemán-Domínguez, M.E., 2020. Additive manufacturing of PLA-based scaffolds intended for bone regeneration and strategies to improve their biological properties. *e-Polymers* 20, 571–599. <https://doi.org/10.1515/epoly-2020-0046>
- Drenckhan, W., Weaire, D., Cox, S.J., 2004. The demonstration of conformal maps with two-dimensional foams. *Eur. J. Phys.* 25, 429. <https://doi.org/10.1088/0143-0807/25/3/010>
- Durand, B., Lebée, A., Seppacher, P., Sab, K., 2022. Predictive strain-gradient homogenization of a pantographic material with compliant junctions. *Journal of the Mechanics and Physics of Solids* 160, 104773. <https://doi.org/10.1016/j.jmps.2021.104773>
- Fernandes, C., Moura, C., Ascenso, R.M.T., Amado, S., Alves, N., Pascoal-Faria, P., 2020. Comprehensive Review on Full Bone Regeneration through 3D Printing Approaches. *Design and Manufacturing*. <https://doi.org/10.5772/intechopen.90864>
- Ganghoffer, J.F., Reda, H., 2021. A variational approach of homogenization of heterogeneous materials towards second gradient continua. *Mechanics of Materials* 158, 103743. <https://doi.org/10.1016/j.mechmat.2021.103743>
- Ghassemi, T., Shahroodi, A., Ebrahimzadeh, M.H., Mousavian, A., Movaffagh, J., Moradi, A., 2018. Current Concepts in Scaffolding for Bone Tissue Engineering. *Arch Bone Jt Surg* 6, 90–99.
- Gibson, L.J., 2005. Biomechanics of cellular solids. *Journal of Biomechanics* 38, 377–399. <https://doi.org/10.1016/j.jbiomech.2004.09.027>

- Goda, I., Ganghoffer, J.-F., 2015. Identification of couple-stress moduli of vertebral trabecular bone based on the 3D internal architectures. *Journal of the Mechanical Behavior of Biomedical Materials* 51, 99–118. <https://doi.org/10.1016/j.jmbbm.2015.06.036>
- Goda, I., Ganghoffer, J.-F., Czarnecki, S., Wawruch, P., Lewiński, T., 2016. Optimal internal architectures of femoral bone based on relaxation by homogenization and isotropic material design. *Mechanics Research Communications* 76, 64–71. <https://doi.org/10.1016/j.mechrescom.2016.06.007>
- Guarino, V., Gloria, A., Raucchi, M.G., Ambrosio, L., 2012. Hydrogel-Based Platforms for the Regeneration of Osteochondral Tissue and Intervertebral Disc. *Polymers* 4, 1590–1612. <https://doi.org/10.3390/polym4031590>
- He, X., Dziak, R., Yuan, X., Mao, K., Genco, R., Swihart, M., Sarkar, D., Li, C., Wang, C., Lu, L., Andreadis, S., Yang, S., 2013. BMP2 Genetically Engineered MSCs and EPCs Promote Vascularized Bone Regeneration in Rat Critical-Sized Calvarial Bone Defects. *PLOS ONE* 8, e60473. <https://doi.org/10.1371/journal.pone.0060473>
- Jackson, C., 2021. Polymeric Scaffolds Used as Prosthetics for Regenerating Tendons. *D.U.Quark* 5, 31–41.
- Jones, A.C., Arns, C.H., Hutmacher, D.W., Milthorpe, B.K., Sheppard, A.P., Knackstedt, M.A., 2009. The correlation of pore morphology, interconnectivity and physical properties of 3D ceramic scaffolds with bone ingrowth. *Biomaterials* 30, 1440–1451. <https://doi.org/10.1016/j.biomaterials.2008.10.056>
- Jungreuthmayer, C., Donahue, S.W., Jaasma, M.J., Al-Munajjed, A.A., Zanghellini, J., Kelly, D.J., O'Brien, F.J., 2009. A comparative study of shear stresses in collagen-glycosaminoglycan and calcium phosphate scaffolds in bone tissue-engineering bioreactors. *Tissue Eng Part A* 15, 1141–1149. <https://doi.org/10.1089/ten.tea.2008.0204>
- Karageorgiou, V., Kaplan, D., 2005. Porosity of 3D biomaterial scaffolds and osteogenesis. *Biomaterials* 26, 5474–5491. <https://doi.org/10.1016/j.biomaterials.2005.02.002>
- Karathanasopoulos, N., Dos Reis, F., Reda, H., Ganghoffer, J.-F., 2018. Computing the effective bulk and normal to shear properties of common two-dimensional architected materials. *Computational Materials Science* 154, 284–294. <https://doi.org/10.1016/j.commatsci.2018.07.044>
- Kolken, H.M.A., Lietaert, K., van der Sloten, T., Pouran, B., Meynen, A., Van Loock, G., Weinans, H., Scheys, L., Zadpoor, A.A., 2020. Mechanical performance of auxetic meta-biomaterials. *Journal of the Mechanical Behavior of Biomedical Materials* 104, 103658. <https://doi.org/10.1016/j.jmbbm.2020.103658>
- Lance, S., Wong, G., 2016. Resorbable Construct for Subtotal Cranial Vault Remodeling. *Annals of Plastic Surgery* 76, S196–S199. <https://doi.org/10.1097/SAP.0000000000000776>
- Langford, T., Mohammed, A., Essa, K., Elshaer, A., Hassanin, H., 2021. 4D Printing of Origami Structures for Minimally Invasive Surgeries Using Functional Scaffold. *Applied Sciences* 11, 332. <https://doi.org/10.3390/app11010332>
- Le, D.T., Marigo, J.-J., 2018. Second order homogenization of quasi-periodic structures. *Vietnam Journal of Mechanics* 40, 325–348. <https://doi.org/10.15625/0866-7136/13498>
- Leszczynska, J., Zyzynska-Granica, B., Koziak, K., Ruminski, S., Lewandowska-Szumiel, M., 2013. Contribution of endothelial cells to human bone-derived cells expansion in coculture. *Tissue Eng Part A* 19, 393–402. <https://doi.org/10.1089/ten.TEA.2011.0710>
- Li, S., Demirci, E., Silberschmidt, V.V., 2013. Variability and anisotropy of mechanical behavior of cortical bone in tension and compression. *Journal of the Mechanical Behavior of Biomedical Materials* 21, 109–120. <https://doi.org/10.1016/j.jmbbm.2013.02.021>
- Li, W., Shanti, R.M., Tuan, R.S., 2006. 135 3 Electrospinning Technology for Nanofibrous Scaffolds in Tissue Engineering.

- Liao, B., Xia, R.F., Li, W., Lu, D., Jin, Z.M., 2021a. 3D-Printed Ti6Al4V Scaffolds with Graded Triply Periodic Minimal Surface Structure for Bone Tissue Engineering. *J. of Materi Eng and Perform* 30, 4993–5004. <https://doi.org/10.1007/s11665-021-05580-z>
- Liao, B., Xia, R.F., Li, W., Lu, D., Jin, Z.M., 2021b. 3D-Printed Ti6Al4V Scaffolds with Graded Triply Periodic Minimal Surface Structure for Bone Tissue Engineering. *J. of Materi Eng and Perform* 30, 4993–5004. <https://doi.org/10.1007/s11665-021-05580-z>
- Limmahakhun, S., Oloyede, A., Sitthiseripratip, K., Xiao, Y., Yan, C., 2017a. Stiffness and strength tailoring of cobalt chromium graded cellular structures for stress-shielding reduction. *Materials & Design* 114, 633–641. <https://doi.org/10.1016/j.matdes.2016.11.090>
- Limmahakhun, S., Oloyede, A., Sitthiseripratip, K., Xiao, Y., Yan, C., 2017b. Stiffness and strength tailoring of cobalt chromium graded cellular structures for stress-shielding reduction. *Materials & Design* 114, 633–641. <https://doi.org/10.1016/j.matdes.2016.11.090>
- Lin, C.Y., Kikuchi, N., Hollister, S.J., 2004. A novel method for biomaterial scaffold internal architecture design to match bone elastic properties with desired porosity. *Journal of Biomechanics* 37, 623–636. <https://doi.org/10.1016/j.jbiomech.2003.09.029>
- Linn, R.V., Oliveira, B.F., 2017. An analytical and numerical framework for evaluating axial compression of finite dimensional metallic foams by generalization of buckling effects. *Mechanics of Advanced Materials and Structures* 24, 1343–1352. <https://doi.org/10.1080/15376494.2016.1227508>
- Liu, F., Mao, Z., Zhang, P., Zhang, D.Z., Jiang, J., Ma, Z., 2018. Functionally graded porous scaffolds in multiple patterns: New design method, physical and mechanical properties. *Materials & Design* 160, 849–860. <https://doi.org/10.1016/j.matdes.2018.09.053>
- Logeart-Avramoglou, D., Anagnostou, F., Bizios, R., Petite, H., 2005. Engineering bone: challenges and obstacles. *Journal of Cellular and Molecular Medicine* 9, 72–84. <https://doi.org/10.1111/j.1582-4934.2005.tb00338.x>
- Louna, Z., Goda, I., Ganghoffer, J.-F., 2019. Homogenized strain gradient remodeling model for trabecular bone microstructures. *Continuum Mech. Thermodyn.* 31, 1339–1367. <https://doi.org/10.1007/s00161-019-00746-6>
- Melchels, F.P.W., Bertoldi, K., Gabbriellini, R., Velders, A.H., Feijen, J., Grijpma, D.W., 2010. Mathematically defined tissue engineering scaffold architectures prepared by stereolithography. *Biomaterials* 31, 6909–6916. <https://doi.org/10.1016/j.biomaterials.2010.05.068>
- Melchiorri, A.J., Nguyen, B.-N.B., Fisher, J.P., 2014. Mesenchymal stem cells: roles and relationships in vascularization. *Tissue Eng Part B Rev* 20, 218–228. <https://doi.org/10.1089/ten.TEB.2013.0541>
- Meng, L., Shi, J., Yang, C., Gao, T., Hou, Y., Song, L., Gu, D., Zhu, J., Breitkopf, P., Zhang, W., 2020. An emerging class of hyperbolic lattice exhibiting tunable elastic properties and impact absorption through chiral twisting. *Extreme Mechanics Letters* 40, 100869. <https://doi.org/10.1016/j.eml.2020.100869>
- Miedzińska, D., 2017. New Method of Numerical Homogenization of Functionally Graded Materials. *Procedia Structural Integrity* 5, 484–491. <https://doi.org/10.1016/j.prostr.2017.07.148>
- Mindlin, R.D., 1964. Micro-structure in linear elasticity. *Arch. Rational Mech. Anal.* 16, 51–78. <https://doi.org/10.1007/BF00248490>
- Nair, L.S., Bhattacharyya, S., Laurencin, C.T., 2007. Nanotechnology and Tissue Engineering: The Scaffold Based Approach, in: Kumar, C.S.S.R. (Ed.), *Nanotechnologies for the Life Sciences*. Wiley-VCH Verlag GmbH & Co. KGaA, Weinheim, Germany, p. ntl0095. <https://doi.org/10.1002/9783527610419.ntls0095>
- Oh, S.H., Park, I.K., Kim, J.M., Lee, J.H., 2007. In vitro and in vivo characteristics of PCL scaffolds with pore size gradient fabricated by a centrifugation method. *Biomaterials* 28, 1664–1671.

<https://doi.org/10.1016/j.biomaterials.2006.11.024>

- Patrick, C.W., Mikos, A.G., McIntire, L.V., 1998. *Frontiers in Tissue Engineering* - 1st Edition [WWW Document]. URL <https://www.elsevier.com/books/frontiers-in-tissue-engineering/patrick/978-0-08-042689-1> (accessed 4.12.22).
- Payne, K.F.B., Balasundaram, I., Deb, S., Di Silvio, L., Fan, K.F.M., 2014. Tissue engineering technology and its possible applications in oral and maxillofacial surgery. *British Journal of Oral and Maxillofacial Surgery* 52, 7–15. <https://doi.org/10.1016/j.bjoms.2013.03.005>
- Peltola, S.M., Melchels, F.P.W., Grijpma, D.W., Kellomäki, M., 2008. A review of rapid prototyping techniques for tissue engineering purposes. *Annals of Medicine* 40, 268–280. <https://doi.org/10.1080/07853890701881788>
- Poh, P.S.P., Valainis, D., Bhattacharya, K., van Griensven, M., Dondl, P., 2019. Optimization of Bone Scaffold Porosity Distributions. *Sci Rep* 9, 9170. <https://doi.org/10.1038/s41598-019-44872-2>
- Qu, H., Fu, H., Han, Z., Sun, Y., 2019. Biomaterials for bone tissue engineering scaffolds: a review. *RSC Adv.* 9, 26252–26262. <https://doi.org/10.1039/C9RA05214C>
- Rüegg, J., Schumacher, R., Weber, F.E., Wild, M. de, 2017. Mechanical anisotropy of titanium scaffolds. *Current Directions in Biomedical Engineering* 3, 607–611. <https://doi.org/10.1515/cdbme-2017-0127>
- Senatov, F.S., Zadorozhnyy, M.Yu., Niaza, K.V., Medvedev, V.V., Kaloshkin, S.D., Anisimova, N.Y., Kiselevskiy, M.V., Yang, K.-C., 2017. Shape memory effect in 3D-printed scaffolds for self-fitting implants. *European Polymer Journal* 93, 222–231. <https://doi.org/10.1016/j.eurpolymj.2017.06.011>
- Shipley, R.J., Jones, G.W., Dyson, R.J., Sengers, B.G., Bailey, C.L., Catt, C.J., Please, C.P., Malda, J., 2009. Design criteria for a printed tissue engineering construct: A mathematical homogenization approach. *Journal of Theoretical Biology* 259, 489–502. <https://doi.org/10.1016/j.jtbi.2009.03.037>
- Sobral, J.M., Caridade, S.G., Sousa, R.A., Mano, J.F., Reis, R.L., 2011. Three-dimensional plotted scaffolds with controlled pore size gradients: Effect of scaffold geometry on mechanical performance and cell seeding efficiency. *Acta Biomaterialia* 7, 1009–1018. <https://doi.org/10.1016/j.actbio.2010.11.003>
- Su, X., Wang, T., Guo, S., 2021. Applications of 3D printed bone tissue engineering scaffolds in the stem cell field. *Regenerative Therapy* 16, 63–72. <https://doi.org/10.1016/j.reth.2021.01.007>
- Tian, Y., Chen, C., Xu, X., Wang, J., Hou, X., Li, K., Lu, X., Shi, H., Lee, E.-S., Jiang, H.B., 2021. A Review of 3D Printing in Dentistry: Technologies, Affecting Factors, and Applications. *Scanning* 2021, 9950131. <https://doi.org/10.1155/2021/9950131>
- Torres-Sanchez, C., Al Mushref, F.R.A., Norrito, M., Yendall, K., Liu, Y., Conway, P.P., 2017. The effect of pore size and porosity on mechanical properties and biological response of porous titanium scaffolds. *Materials Science and Engineering: C* 77, 219–228. <https://doi.org/10.1016/j.msec.2017.03.249>
- Wang, C., Huang, W., Zhou, Y., He, L., He, Z., Chen, Z., He, X., Tian, S., Liao, J., Lu, B., Wei, Y., Wang, M., 2020. 3D printing of bone tissue engineering scaffolds. *Bioactive Materials* 5, 82–91. <https://doi.org/10.1016/j.bioactmat.2020.01.004>
- Weisgrab, G., Guillaume, O., Guo, Z., Heimel, P., Slezak, P., Poot, A., Grijpma, D., Ovsianikov, A., 2020. 3D Printing of large-scale and highly porous biodegradable tissue engineering scaffolds from poly(trimethylene-carbonate) using two-photon-polymerization. *Biofabrication* 12, 045036. <https://doi.org/10.1088/1758-5090/abb539>
- Xin, X., Liu, L., Liu, Y., Leng, J., 2020. 4D Printing Auxetic Metamaterials with Tunable, Programmable, and Reconfigurable Mechanical Properties. *Advanced Functional Materials* 30, 2004226. <https://doi.org/10.1002/adfm.202004226>
- Xu, L., Qian, Z., 2021. Topology optimization and de-homogenization of graded lattice structures based on

asymptotic homogenization. *Composite Structures* 277, 114633.
<https://doi.org/10.1016/j.compstruct.2021.114633>

Yoo, D.J., 2011. Porous scaffold design using the distance field and triply periodic minimal surface models. *Biomaterials* 32, 7741–7754. <https://doi.org/10.1016/j.biomaterials.2011.07.019>

Yook, S.-W., Jung, H.-D., Park, C.-H., Shin, K.-H., Koh, Y.-H., Estrin, Y., Kim, H.-E., 2012. Reverse freeze casting: A new method for fabricating highly porous titanium scaffolds with aligned large pores. *Acta Biomaterialia* 8, 2401–2410. <https://doi.org/10.1016/j.actbio.2012.03.020>

Zadpoor, A.A., 2015. Bone tissue regeneration: the role of scaffold geometry. *Biomater. Sci.* 3, 231–245. <https://doi.org/10.1039/C4BM00291A>

Zhou, X., Jin, Y., Du, J., 2020. Functionally Graded Scaffolds with Programmable Pore Size Distribution Based on Triply Periodic Minimal Surface Fabricated by Selective Laser Melting. *Materials* 13, 5046. <https://doi.org/10.3390/ma13215046>